Software: HEASOFT (NASA High Energy Astrophysics Science Archive Research Center (Heasarc), 2014); BATANALYSIS (T. Parsotan et al. 2023, in preparation); XSPEC (Arnaud 1996); ASTROPY (Astropy Collaboration et al. 2013); EMCEE (Foreman-Mackey et al. 2019).

Appendix A
BAT Survey Mode and Mosaic Flux Measurements

Details of the flux measurements and upper limits obtained from the Swift BAT survey mode data are shown in Table 3, and the results of the daily mosaicing are presented in Table 4.

Table 3
BAT Survey Observations of GRB 221009A

Obs ID	Pointing ID	$T_{start} - T_0$ (ks)	UTC Time	Exposure (ks)	14–195 keV Flux (erg cm^{-2} s^{-1})	Photon Index
03111868007	20222810634	−110.5	2022 Oct 8 06:34:32	0.661	$<1.11 \times 10^{-8}$	⋯
	20222821110	−7.6	2022 Oct 9 11:10:19	0.373	$<1.55 \times 10^{-8}$	⋯
00015314118	20222820117	−43.2	2022 Oct 9 01:17:08	0.924	$<6.33 \times 10^{-9}$	⋯
00046390010	20222820135	−42.1	2022 Oct 9 01:34:40	0.172	$<3.34 \times 10^{-8}$	⋯
00015314119	20222820626	−24.6	2022 Oct 9 06:26:19	0.900	$<6.36 \times 10^{-9}$	⋯
00015357004	20222820921	−14.1	2022 Oct 9 09:21:28	0.544	$<1.42 \times 10^{-8}$	⋯
00011105067	20222821046	−9.1	2022 Oct 9 10:46:08	1.344	$<1.36 \times 10^{-8}$	⋯
00015314120	20222821248	−1.7	2022 Oct 9 12:48:26	0.846	$<7.14 \times 10^{-9}$	⋯
01126854000	20222821422	3.9	2022 Oct 9 14:22:05	0.627	$3.22^{+0.38}_{-0.37} \times 10^{-8}$	$2.13^{+0.19}_{-0.19}$
01126853001	20222821917	21.6	2022 Oct 9 19:17:08	0.500	$2.61^{+0.93}_{-0.86} \times 10^{-9}$	$1.81^{+0.44}_{-0.44}$
01126853003	20222822027	25.8	2022 Oct 9 20:26:45	0.900	$2.44^{+0.66}_{-0.62} \times 10^{-9}$	$2.31^{+0.52}_{-0.51}$
00015314121	20222822047	27.0	2022 Oct 9 20:46:57	0.755	$3.01^{+1.11}_{-1.02} \times 10^{-9}$	$1.53^{+0.57}_{-0.54}$
01126853004	20222822156	31.1	2022 Oct 9 21:55:37	1.744	$1.73^{+0.55}_{-0.5} \times 10^{-9}$	$1.85^{+0.49}_{-0.48}$
	20222822332	36.9	2022 Oct 9 23:31:40	1.500	$<4.09 \times 10^{-9}$	⋯
	20222830129	43.9	2022 Oct 10 01:29:08	1.073	$<4.76 \times 10^{-9}$	⋯
	20222830243	48.4	2022 Oct 10 02:43:05	1.742	$<3.82 \times 10^{-9}$	⋯
	20222830417	54.0	2022 Oct 10 04:16:45	1.738	$<3.74 \times 10^{-9}$	⋯
	20222830754	67.0	2022 Oct 10 07:53:52	0.914	$<5.05 \times 10^{-9}$	⋯
	20222830934	73.0	2022 Oct 10 09:34:21	0.514	$<6.78 \times 10^{-9}$	⋯
	20222831234	83.8	2022 Oct 10 12:33:38	1.314	$<4.61 \times 10^{-9}$	⋯
	20222831354	88.6	2022 Oct 10 13:53:49	1.183	$<4.81 \times 10^{-9}$	⋯
	20222831531	94.4	2022 Oct 10 15:30:56	0.900	$<5.34 \times 10^{-9}$	⋯
	20222831550	95.6	2022 Oct 10 15:50:56	0.543	$<6.53 \times 10^{-9}$	⋯
	20222831704	100.0	2022 Oct 10 17:04:26	1.679	$<3.76 \times 10^{-9}$	⋯
03111808004	20222830447	55.8	2022 Oct 10 04:46:38	0.594	$<5.99 \times 10^{-9}$	⋯
00033349157	20222830906	71.3	2022 Oct 10 09:05:56	1.655	$<3.68 \times 10^{-9}$	⋯
00015314124	20222831417	90.0	2022 Oct 10 14:17:05	0.807	$<7.28 \times 10^{-9}$	⋯
01126853005	20222831837	105.6	2022 Oct 10 18:37:15	1.500	$<3.80 \times 10^{-9}$	⋯
00015314125	20222831904	107.2	2022 Oct 10 19:03:48	0.704	$<7.11 \times 10^{-9}$	⋯
01126853006	20222832022	111.9	2022 Oct 10 20:22:19	1.500	$<4.07 \times 10^{-9}$	⋯
	20222832147	117.0	2022 Oct 10 21:47:19	0.900	$<5.17 \times 10^{-9}$	⋯
	20222832204	118.2	2022 Oct 10 22:07:19	0.299	$<8.71 \times 10^{-9}$	⋯
	20222840108	129.1	2022 Oct 11 01:08:33	0.839	$<5.31 \times 10^{-9}$	⋯
	20222840233	134.2	2022 Oct 11 02:33:30	0.782	$<5.24 \times 10^{-9}$	⋯
	20222840444	142.0	2022 Oct 11 04:44:25	0.362	$<8.01 \times 10^{-9}$	⋯
	20222840548	145.8	2022 Oct 11 05:47:44	1.499	$<3.98 \times 10^{-9}$	⋯
	20222840735	152.3	2022 Oct 11 07:34:38	1.500	$<4.04 \times 10^{-9}$	⋯
	20222840915	158.3	2022 Oct 11 09:14:53	1.254	$<4.59 \times 10^{-9}$	⋯
	20222841047	163.8	2022 Oct 11 10:47:19	1.453	$<4.26 \times 10^{-9}$	⋯
00015314126	20222840250	135.2	2022 Oct 11 02:50:06	0.806	$<7.35 \times 10^{-9}$	⋯
00015314127	20222840858	157.3	2022 Oct 11 08:58:33	0.899	$<6.83 \times 10^{-9}$	⋯

Note. Upper limits are calculated with an assumed photon index of 1.

Table 4
Swift BAT Daily and Total Mosaics of GRB 221009A

Start Time Bin	End Time Bin	Exposure (ks)	14–195 keV Flux (erg cm^{-2} s^{-1})	Photon Index
2022 Oct 8	2022 Oct 9	0.661	$<2.63 \times 10^{-9}$	...
2022 Oct 9	2022 Oct 10	6.541	$5.05^{+0.29}_{-0.29} \times 10^{-9}$	$2.30^{+0.09}_{-0.09}$
2022 Oct 10	2022 Oct 11	7.710	$6.68^{+2.4}_{-2.1} \times 10^{-10}$	$2.43^{+0.61}_{-0.51}$
2022 Oct 11	2022 Oct 12	4.136	$<6.47 \times 10^{-10}$	...
2022 Oct 8	2022 Oct 12	19.048	$1.90^{+0.17}_{-0.17} \times 10^{-9}$	$2.28^{+0.15}_{-0.14}$

Note. Upper limits are calculated with an assumed photon index of 1.

Appendix B
Swift XRT Dust and Background Subtraction

In WT mode, the Swift XRT CCD is read out in columns, and the spatial information is collapsed to one single dimension. As a result, the *source* region will contain all dust photons *above* and *below* the GRB in terms of CCD position, while the background regions will sample a different vertical slice through the dust rings, with potentially different spectral properties from those in the source region. Furthermore, the columns are summed over the full 600 pixel height of the XRT CCD, but only the central 200 columns are read out, which can make a suitable background region difficult to obtain.

Example time-sliced 1D profiles from the WT-mode data are shown in Figure 7. These suggest that within a 20 pixel source accumulation region, the data are dominated by the source. The profile from the first snapshot of WT data is shown in more detail in Figure 8, along with a fit of the profile expected from a point source; the lower panel shows the difference between the data and model. As the GRB was so bright in this snapshot, the central core profile is suppressed due to pile-up (resulting in a negative residual, which is not shown for clarity); the central 10 columns were subsequently excluded in the spectral extraction to remove the piled-up core. The remaining residuals suggest the scattering echoes contribute ∼10%–15% of the observed count rate in a 5–20 pixel radius extraction region centered on the source; thus the GRB spectral normalization will be overestimated by a similar amount due to the echo contamination in this snapshot.

To investigate the effect of the echo on the subsequent WT-mode flux measurements, we took the PC-mode image from $T_0 + 1.036 - 1.111$ days and summed it in 1D so as to mimic the WT-mode profiles. We did this twice; first using all data, then a second time after removing a model of the central source PSF, which was fit to the innermost 20 pixel radius data. The 1D intensity profiles thus obtained show the sourceless data are approximately flat, with a variation of <25% between the source outer extraction radius and the wings out to 6′. Within the source accumulation region, ∼75% of the events come from the source. Thus, the source light curve is not significantly altered by the variation in the estimated background level obtained from the wings of the 1D profile where the dust dominates.

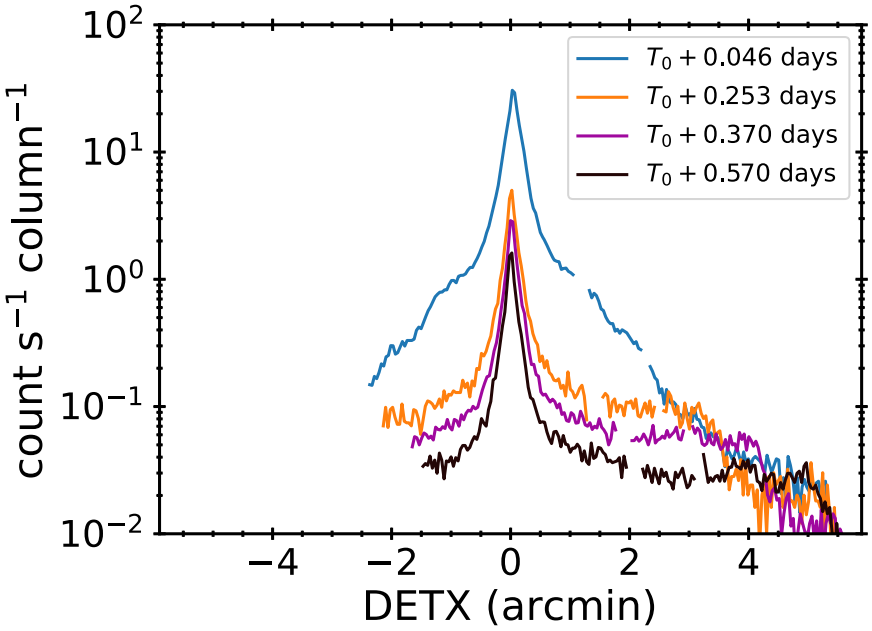

Figure 7. XRT WT-mode 1D PSF profiles as a function of time in the 0.8–5.0 keV band, illustrating the evolution of the echo in the early WT data.

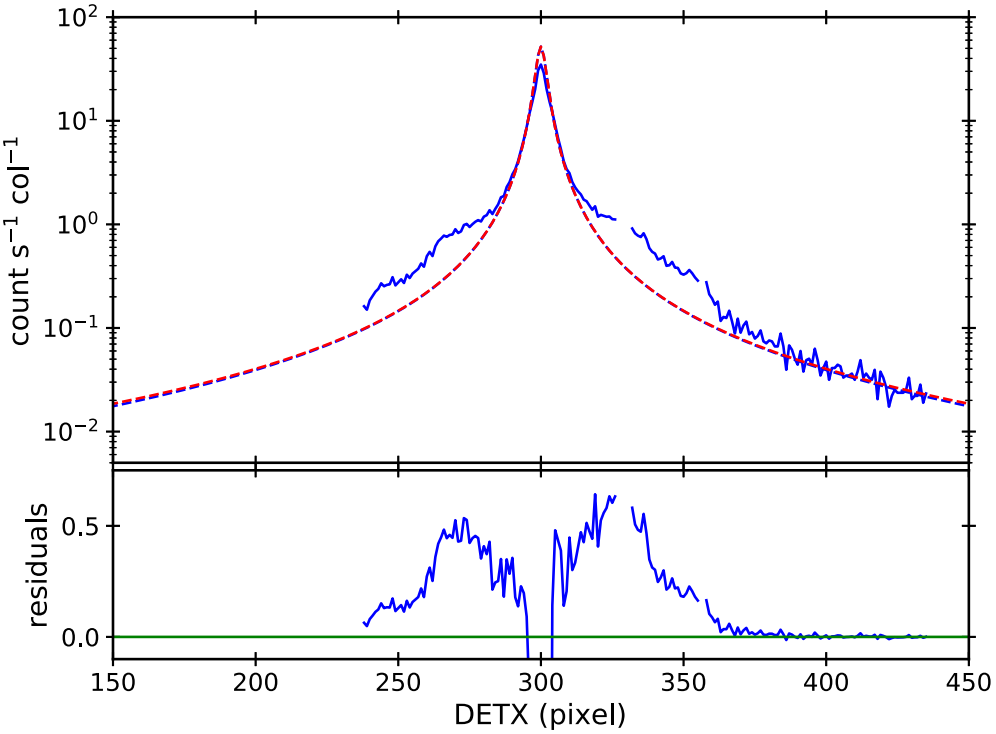

Figure 8. Upper panel: XRT WT-mode 1D PSF profile from the first snapshot of data at $T_0 + 3.4$ ks (solid line) and the modeled point-source profile (dashed line). Lower panel: the data minus model residual.

To determine the impact of dust on the WT-mode spectroscopic data, we used the PC-mode data in ObsID 01126853004, comprising 3.1 ks of data collected between 89 and 101 ks after the Fermi trigger.[45] First we extracted data from a vertical region corresponding to a typical WT-mode background region, and also from a 20 column radius region around the source, excluding the source itself. The spectrum of the dust in the source columns is visibly slightly harder than that in the background region; fitting an absorbed power law in XSPEC showed the difference to be minimal, however, with the best-fitting parameters varying by less than 6% between the two spectra and comfortably agreeing within their 90% confidence errors. To better quantify the effect of this possible change in dust spectrum between source and background regions, we extracted two spectra from the PC-mode data. The first was taken from a 20 pixel radius circle centered on the source (i.e., with no dust present) with a background spectrum taken from the dust-free region identified above. In the second case, we mimicked WT data, extracting data from the full vertical height of the CCD for regions corresponding to those used in the WT-mode analysis (Figure 9). We fit these two spectra independently in XSPEC using the absorbed power-law

[45] Although the first snapshot from this ObsID started at 68 ks, its on time was only 7.5 s, meaning the exposure effectively started during the second snapshot at 89 ks post trigger.

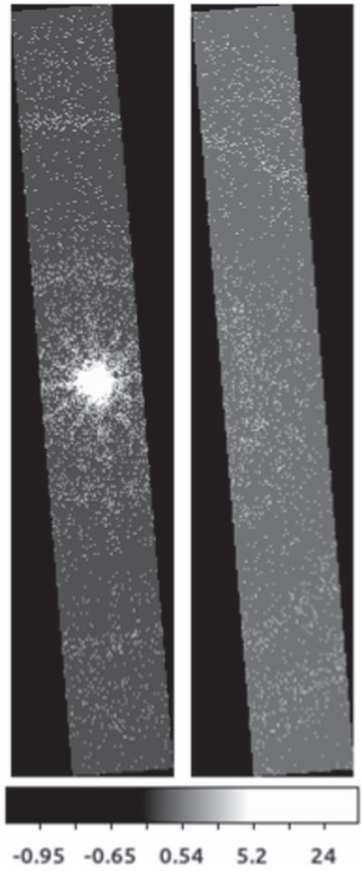

Figure 9. The extracted PC-mode data designed to mimic the WT-mode extraction to investigate the impact of dust. Left: the source region. Right: the background region. The regions are tilted at the roll angle of the spacecraft.

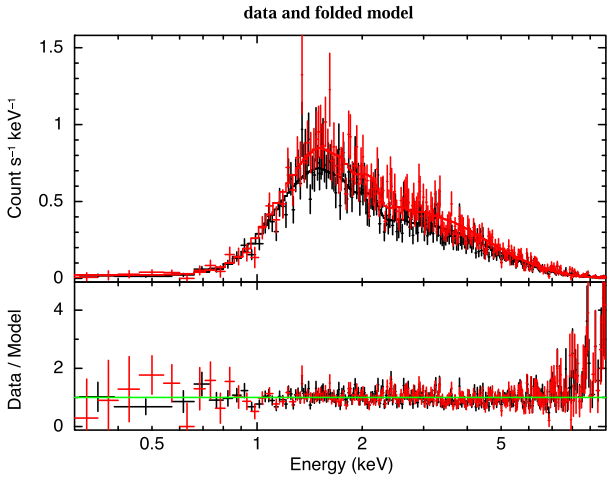

Figure 10. A comparison of a PC-mode spectrum (black), in which dust has been correctly accounted for, and a mimicked WT-mode spectrum (red) of the same data, enabling us to quantify the impact of the dust on the WT-mode data.

model. The results are shown in Table 5 and in Figure 10. While all parameters agree to within their errors, the best-fit photon index is 7% higher (i.e., softer), and the absorption column is 27% higher in the WT-style data. Since these data were gathered when the source was fainter than in the real WT data (i.e., the impact of dust contamination is at its worst in this experiment), we adopt these percentages as the maximum inaccuracy expected from our WT-mode spectral fits.

Table 5
An Estimate of the Impact of Dust on the WT-mode Spectral Fit Results; See Text for Details

Parameter	PC Result	Pseudo-WT Result	Percentage Difference[a]
$N_{\rm H}$ (10^{22} cm^{-2})	1.1 ± 0.2	1.4 ± 0.2	27%
Photon index	1.47 ± 0.08	1.57 ± 0.09	7%
Flux (0.3–10 keV, 10^{-10} erg cm^{-2} s^{-1})	1.64 ± 0.06	1.74 ± 0.06	6%

Note.
[a] (PC-WT)/PC.

Appendix C
UVOT Afterglow Photometry

The final photometry measured for GRB 221009A is displayed in Table 6.

Table 6
Swift UVOT Observations

$T_{\rm mid} - T_0$ (ks)	Half Exposure (s)	Magnitude	Flux (erg cm^{-2} s^{-1} Å^{-1})	Filter	S/N
3.4	25	$16.743^{+0.051}_{-0.048}$	$9.64 \pm 0.44 \times 10^{-16}$	*white*	21.956
3.5	30	$16.762^{+0.046}_{-0.045}$	$9.48 \pm 0.40 \times 10^{-16}$	*white*	23.877
3.5	20	$16.726^{+0.057}_{-0.054}$	$9.80 \pm 0.50 \times 10^{-16}$	*white*	19.698
3.8	10	$16.71^{+0.097}_{-0.089}$	$9.94 \pm 0.85 \times 10^{-16}$	*white*	11.664
4.0	10	$16.958^{+0.103}_{-0.094}$	$7.91 \pm 0.72 \times 10^{-16}$	*white*	11.024
4.1	75	$16.972^{+0.075}_{-0.07}$	$7.81 \pm 0.52 \times 10^{-16}$	*white*	15.078
4.4	10	$16.976^{+0.104}_{-0.095}$	$7.78 \pm 0.71 \times 10^{-16}$	*white*	10.976
21.9	246	$18.803^{+0.063}_{-0.06}$	$1.45 \pm 0.08 \times 10^{-16}$	*white*	17.686
44.9	76	$19.862^{+0.166}_{-0.144}$	$5.45 \pm 0.77 \times 10^{-17}$	*white*	7.065
61.2	408	$20.1^{+0.085}_{-0.079}$	$4.38 \pm 0.33 \times 10^{-17}$	*white*	13.261
120.0	14,394	$21.152^{+0.079}_{-0.074}$	$1.66 \pm 0.12 \times 10^{-17}$	*white*	14.176
152.3	17,859	$21.655^{+0.099}_{-0.09}$	$1.05 \pm 0.09 \times 10^{-17}$	*white*	11.522
198.5	23,982	$21.599^{+0.21}_{-0.176}$	$1.10 \pm 0.19 \times 10^{-17}$	*white*	5.685
258.6	31,606	$21.987^{+0.19}_{-0.162}$	$7.71 \pm 1.24 \times 10^{-18}$	*white*	6.218
306.9	6602	$22.574^{+0.324}_{-0.249}$	$4.49 \pm 1.16 \times 10^{-18}$	*white*	3.872
436.1	49,190	$22.703^{+0.486}_{-0.334}$	$3.99 \pm 1.44 \times 10^{-18}$	*white*	2.773
585.3	71,725	$22.688^{+0.543}_{-0.36}$	$4.04 \pm 1.59 \times 10^{-18}$	*white*	2.541
754.3	91,946	$22.594^{+0.573}_{-0.373}$	$4.41 \pm 1.81 \times 10^{-18}$	*white*	2.440
971.9	120,245	>22.625	$<4.28 \times 10^{-18}$	*white*	⋯
1251.6	154,713	>22.882	$< 3.38 \times 10^{-18}$	*white*	⋯
1701.2	192,141	>22.836	$< 3.52 \times 10^{-18}$	*white*	⋯
2087.8	137,716	>23.166	$< 2.60 \times 10^{-18}$	*white*	⋯
3940.8	432,429	>23.602	$< 1.74 \times 10^{-18}$	*white*	⋯
3.4	5	$15.463^{+0.162}_{-0.141}$	$2.44 \pm 0.34 \times 10^{-15}$	*v*	7.210
3.9	10	$15.538^{+0.125}_{-0.112}$	$2.28 \pm 0.25 \times 10^{-15}$	*v*	9.220
4.2	114	$15.729^{+0.094}_{-0.086}$	$1.91 \pm 0.16 \times 10^{-15}$	*v*	12.072
4.4	10	$15.893^{+0.145}_{-0.128}$	$1.64 \pm 0.21 \times 10^{-15}$	*v*	7.995
38.2	412	$18.152^{+0.077}_{-0.072}$	$2.05 \pm 0.14 \times 10^{-16}$	*v*	14.642
55.3	412	$18.755^{+0.11}_{-0.1}$	$1.18 \pm 0.11 \times 10^{-16}$	*v*	10.375
92.8	8959	$19.427^{+0.123}_{-0.11}$	$6.34 \pm 0.68 \times 10^{-17}$	*v*	9.342
436.6	49,188	>20.443	$< 2.49 \times 10^{-17}$	*v*	⋯
573.7	59,918	$21.082^{+0.698}_{-0.421}$	$1.38 \pm 0.66 \times 10^{-17}$	*v*	2.109
822.1	97,374	>20.64	$< 2.08 \times 10^{-17}$	*v*	⋯
1065.7	122,800	>21.411	$< 1.02 \times 10^{-17}$	*v*	⋯
1372.4	160,437	>21.617	$< 8.44 \times 10^{-18}$	*v*	⋯
1833.6	220,177	>22.032	$< 5.76 \times 10^{-18}$	*v*	⋯
2151.2	74,786	>21.125	$< 1.33 \times 10^{-17}$	*v*	⋯
3940.0	432,472	>21.862	$< 6.74 \times 10^{-18}$	*v*	⋯
3.8	10	$17.062^{+0.144}_{-0.127}$	$9.70 \pm 1.20 \times 10^{-16}$	*b*	8.058
4.0	10	$17.227^{+0.155}_{-0.136}$	$8.34 \pm 1.11 \times 10^{-16}$	*b*	7.495
4.4	92	$17.551^{+0.144}_{-0.127}$	$6.18 \pm 0.77 \times 10^{-16}$	*b*	8.073
44.4	454	$20.268^{+0.145}_{-0.128}$	$5.06 \pm 0.63 \times 10^{-17}$	*b*	7.999
60.3	453	$20.666^{+0.237}_{-0.194}$	$3.51 \pm 0.69 \times 10^{-17}$	*b*	5.100
438.9	52,551	>21.71	$< 1.34 \times 10^{-17}$	*b*	⋯
584.9	71,610	>21.597	$< 1.49 \times 10^{-17}$	*b*	⋯
753.8	92,017	$22.444^{+0.512}_{-0.346}$	$6.82 \pm 2.56 \times 10^{-18}$	*b*	2.662
971.7	120,321	>22.02	$< 1.01 \times 10^{-17}$	*b*	⋯
1251.2	154,869	>22.124	$< 9.16 \times 10^{-18}$	*b*	⋯
1700.9	192,324	>22.229	$< 8.32 \times 10^{-18}$	*b*	⋯
2087.2	137,713	>22.48	$< 6.60 \times 10^{-18}$	*b*	⋯
3849.4	438,307	>22.969	$< 4.21 \times 10^{-18}$	*b*	⋯
3.6	38	$17.592^{+0.129}_{-0.115}$	$3.24 \pm 0.36 \times 10^{-16}$	*u*	8.927
3.7	50	$17.673^{+0.115}_{-0.104}$	$3.01 \pm 0.30 \times 10^{-16}$	*u*	9.933
3.7	37	$17.629^{+0.131}_{-0.117}$	$3.13 \pm 0.36 \times 10^{-16}$	*u*	8.773
3.9	10	$17.882^{+0.309}_{-0.24}$	$2.48 \pm 0.61 \times 10^{-16}$	*u*	4.041
4.4	97	$17.765^{+0.196}_{-0.166}$	$2.77 \pm 0.46 \times 10^{-16}$	*u*	6.043
32.4	415	$20.258^{+0.207}_{-0.174}$	$2.78 \pm 0.48 \times 10^{-17}$	*u*	5.769

Table 6
(Continued)

$T_{\rm mid} - T_0$ (ks)	Half Exposure (s)	Magnitude	Flux (erg cm^{-2} s^{-1} Å^{-1})	Filter	S/N
49.7	414	$20.729^{+0.313}_{-0.243}$	$1.80 \pm 0.45 \times 10^{-17}$	*u*	3.992
95.8	414	$21.106^{+0.438}_{-0.311}$	$1.27 \pm 0.42 \times 10^{-17}$	*u*	3.010
438.8	52,496	>20.903	$< 1.54 \times 10^{-17}$	*u*	⋯
584.7	71,385	>20.647	$< 1.94 \times 10^{-17}$	*u*	⋯
753.5	91,837	>21.678	$< 7.52 \times 10^{-18}$	*u*	⋯
971.4	120,396	>21.285	$< 1.08 \times 10^{-17}$	*u*	⋯
1251.1	154,783	>21.32	$< 1.05 \times 10^{-17}$	*u*	⋯
1700.8	192,285	>21.335	$< 1.03 \times 10^{-17}$	*u*	⋯
2086.9	137,473	>20.098	$< 3.23 \times 10^{-17}$	*u*	⋯
3848.7	438,428	>22.798	$<2.68 \times 10^{-18}$	*u*	⋯
3.9	10	$18.238^{+0.671}_{-0.412}$	$2.02 \pm 0.93 \times 10^{-16}$	*uvw1*	2.168
4.4	97	>19.108	$< 9.06 \times 10^{-17}$	*uvw1*	⋯
31.6	450	>20.175	$< 3.39 \times 10^{-17}$	*uvw1*	⋯
48.8	450	>20.003	$< 3.97 \times 10^{-17}$	*uvw1*	⋯
67.5	450	>20.5	$< 2.51 \times 10^{-17}$	*uvw1*	⋯
92.4	2910	>21.471	$< 1.03 \times 10^{-17}$	*uvw1*	⋯
685.4	269	>20.833	$< 1.85 \times 10^{-17}$	*uvw1*	⋯
1458.7	22,863	>22.436	$< 4.23 \times 10^{-18}$	*uvw1*	⋯
3.9	10	>18.228	$< 2.37 \times 10^{-16}$	*uvm2*	⋯
4.4	97	>18.771	$< 1.44 \times 10^{-16}$	*uvm2*	⋯
87.1	2398	>21.314	$< 1.38 \times 10^{-17}$	*uvm2*	⋯
3.9	10	>18.852	$< 1.54 \times 10^{-16}$	*uvw2*	⋯
4.1	114	>19.356	$< 9.68 \times 10^{-17}$	*uvw2*	⋯
4.4	10	>18.966	$< 1.39 \times 10^{-16}$	*uvw2*	⋯
25.6	83	>19.614	$< 7.64 \times 10^{-17}$	*uvw2*	⋯
37.3	450	>20.917	$< 2.30 \times 10^{-17}$	*uvw2*	⋯
54.4	450	>20.68	$< 2.86 \times 10^{-17}$	*uvw2*	⋯
73.3	253	>21.153	$< 1.85 \times 10^{-17}$	*uvw2*	⋯
100.5	450	>20.525	$< 3.30 \times 10^{-17}$	*uvw2*	⋯

Note. Columns (1) and (2) give the midtime of the exposure in kiloseconds since the GBM trigger and the length of the exposure divided by 2. Magnitudes are given in the Vega system. Uncertainties are given at the 1σ level. Observations with S/N greater than or equal to 2 were considered detections. For the nondetections, 3σ upper limits are given. The values in this table have not been corrected for Galactic extinction.

Appendix D
MAXI Spectral Analysis and Dust Scattering Mitigation

Source spectra at the first ($T_0 + 2.5$ ks) and second ($T_0 + 8.0$ ks) scans were extracted from a $3.^{\circ}0 \times 4.^{\circ}0$ rectangular region centered on the source (Figure 11, left), corresponding to the FWHM of 1.5° and 1.5°–2° of the PSF for the scan and its perpendicular (anode) directions, respectively (Sugizaki et al. 2011). Since the source was detected near the center of the GSC_4 detector and at the edge of the GSC_5 detector ($\beta = 2^{\circ}$–3°; see Figure 2 in Mihara et al. 2011), we extracted the background spectra from two $2.^{\circ}4 \times 4.^{\circ}0$ rectangular regions before and after scanning the source region, avoiding a shadow region near the center frame of the GSC_4 camera body (at $\beta \simeq 0$) and a high background region in the GSC_5. GSC_4 spectra at or after the scan at 17:04 ($T_0 + 13.6$ ks) were obtained from a circular region within a radius of $1.^{\circ}5$, and the background ones were from an annulus region with the inner and outer radii of $2.^{\circ}0$ and $4.^{\circ}0$ overlapped with a $8.^{\circ}0 \times 3.^{\circ}4$ rectangular region (Figure 11, right). GSC_5 spectra at those scans were not used because of low signal-to-noise data.

We evaluated fluxes of the direct afterglow component in the following two ways: First, we fitted the spectra in the 4–20 keV band where the contribution from the dust scattering component is small (middle rows in Table 7). This led to harder fitted photon indices in the first and second scan spectra, $\Gamma = 1.75 \pm 0.09$, and $\Gamma = 2.07^{+0.28}_{-0.26}$, than those in the simple 2–20 keV fits, the former being closer to that of the first XRT observation, 1.61 ± 0.02.

Next we directly investigated energy spectra of the dust scattering component using the XRT data. To emulate the dust scattering spectrum, we fit the XRT spectra of two bright outer dust-echo rings at $T_0 + 95.4$ ks and $T_0 + 146.7$ ks with the above power-law model with the fixed column densities. The resultant weighted mean power-law spectral index is $\Gamma_{\rm dust} = 3.94 \pm 0.04$. Assuming this value does not change with time, we attempted to fit the GSC spectra at 2–20 keV with a model with two power laws, allowing the normalization of both components and the nondust photon index for the first and second scan spectra to be free (Figure 12). We summarize the fitting results in the lower rows in Table 7. Interestingly, the obtained parameters for the first and second scan spectra are almost perfectly consistent with those in the single power-law fits at 4–20 keV whether the photon index is fixed or not; though the uncertainty of the dust flux (the normalization of the power law with $\Gamma = 3.94$) is large. We also note that the first

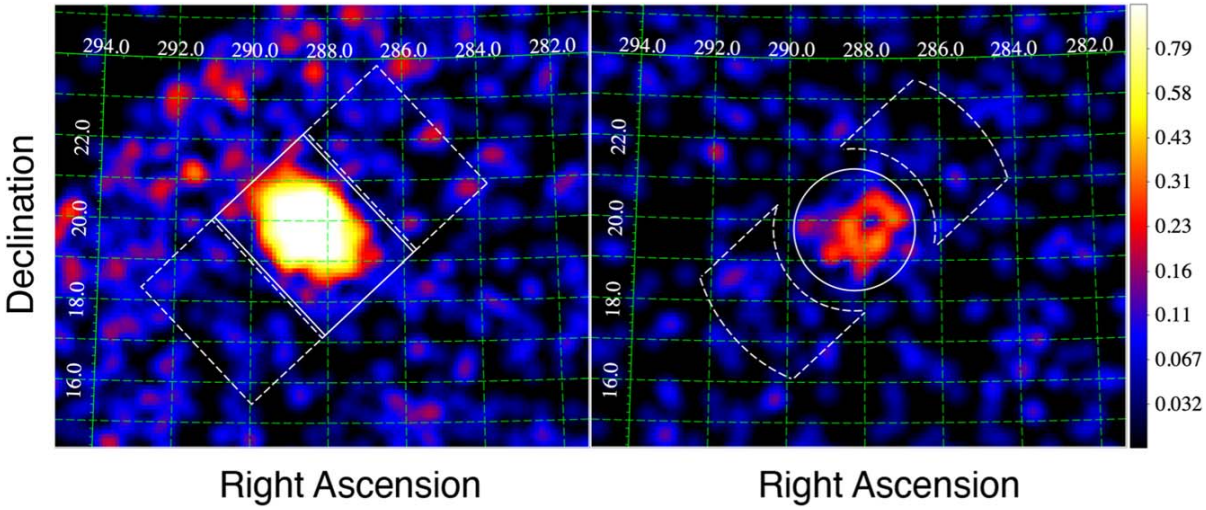

Figure 11. GSC 2–20 keV images obtained with GSC_5 at $T_0 + 2.5$ ks (left) and GSC_4 at $T_0 + 13.6$ ks (right). Source and background regions are shown by the solid lines and the dashed lines, respectively.

Table 7
MAXI Observation Logs and Spectral Fit Results

$T - T_0$ (ks)	Photon Index	Flux (10^{-8} erg cm^{-2} s^{-1}) 0.3–10 keV	Flux (10^{-8} erg cm^{-2} s^{-1}) unabs 0.3–10 keV	Flux (10^{-8} erg cm^{-2} s^{-1}) 4–10 keV	Dust Flux 0.3–10 keV	C-stat/d.o.f.
Single power-law fit (range: 2–20 keV)						
2.459	1.95 ± 0.05	6.98 ± 0.21	$13.54^{+0.85}_{-0.78}$	3.68 ± 0.11	⋯	353/367
	1.85 [f]	6.83 ± 0.19	12.32 ± 0.34	$3.77^{+0.11}_{-0.10}$	⋯	356/368
8.033	$2.22^{+0.16}_{-0.15}$	$1.31^{+0.10}_{-0.09}$	$3.21^{+0.68}_{-0.51}$	0.60 ± 0.05	⋯	180/208
	1.85 [f]	$1.22^{+0.09}_{-0.08}$	2.21 ± 0.15	0.68 ± 0.05	⋯	187/209
13.608	1.85 [f]	0.66 ± 0.08	$1.19^{+0.15}_{-0.14}$	$0.36^{+0.05}_{-0.04}$	⋯	93/84
19.181	1.85 [f]	0.45 ± 0.07	$0.80^{+0.13}_{-0.12}$	0.25 ± 0.04	⋯	59/62
24.757	1.85 [f]	$0.37^{+0.07}_{-0.06}$	$0.66^{+0.12}_{-0.11}$	$0.20^{+0.04}_{-0.03}$	⋯	40/51
30.330	1.85 [f]	0.12 ± 0.06	$0.22^{+0.11}_{-0.10}$	0.07 ± 0.03	⋯	54/37
Single power-law fit (range: 4–20 keV)						
2.459	1.75 ± 0.09	$6.01^{+0.36}_{-0.34}$	$10.10^{+1.18}_{-1.01}$	3.46 ± 0.13	⋯	307/322
	1.85 [f]	6.34 ± 0.23	$11.44^{+0.42}_{-0.41}$	$3.50^{+0.13}_{-0.12}$	⋯	309/323
8.033	$2.07^{+0.28}_{-0.26}$	$1.17^{+0.22}_{-0.18}$	$2.52^{+1.35}_{-0.74}$	0.58 ± 0.06	⋯	145/166
	1.85 [f]	1.05 ± 0.10	$1.90^{+0.19}_{-0.18}$	0.58 ± 0.06	⋯	146/167
13.608	1.85 [f]	0.60 ± 0.12	$1.08^{+0.22}_{-0.21}$	$0.33^{+0.07}_{-0.06}$	⋯	42/36
19.181	1.85 [f]	$0.36^{+0.09}_{-0.08}$	$0.65^{+0.16}_{-0.14}$	$0.20^{+0.05}_{-0.04}$	⋯	43/41
24.757	1.85 [f]	0.30 ± 0.08	$0.55^{+0.15}_{-0.14}$	$0.17^{+0.05}_{-0.04}$	⋯	29/33
30.330	1.85 [f]	$0.13^{+0.09}_{-0.08}$	$0.24^{+0.16}_{-0.15}$	$0.07^{+0.05}_{-0.04}$	⋯	52/32
Two power-law fit						
2.459	1.81 ± 0.12	$6.16^{+0.63}_{-0.57}$	$10.79^{+2.09}_{-1.66}$	$3.47^{+0.20}_{-0.19}$	$1.18^{+0.81}_{-0.87}$	351/366
	1.85 [f]	$6.36^{+0.28}_{-0.27}$	$11.48^{+0.50}_{-0.49}$	3.51 ± 0.15	$0.91^{+0.42}_{-0.41}$	351/367
8.033	$2.14^{+0.16}_{-0.38}$	$1.22^{+0.18}_{-0.33}$	$2.81^{+0.92}_{-1.27}$	$0.59^{+0.07}_{-0.09}$	$0.11^{+0.48}_{-0.11}$	180/207
	1.85 [f]	0.98 ± 0.13	1.77 ± 0.23	0.54 ± 0.07	$0.46^{+0.20}_{-0.19}$	181/208
13.608	1.85 [f]	$0.53^{+0.13}_{-0.12}$	$0.95^{+0.23}_{-0.22}$	0.29 ± 0.07	$0.24^{+0.20}_{-0.18}$	92/83
19.181	1.85 [f]	$0.27^{+0.11}_{-0.10}$	$0.49^{+0.10}_{-0.18}$	$0.15^{+0.06}_{-0.05}$	$0.32^{+0.17}_{-0.16}$	55/61
24.757	1.85 [f]	$0.25^{+0.10}_{-0.09}$	$0.46^{+0.18}_{-0.17}$	0.14 ± 0.05	$0.22^{+0.17}_{-0.15}$	38/50
30.330	1.85 [f]	0.12 ± 0.06	0.22 ± 0.11	$0.07^{+0.03}_{-0.04}$	0.00 ± 0.00	54/36

Note. Flux columns show observed flux at 0.3–10 keV, unabsorbed flux at 0.3–10 keV, and observed flux at 4–10 keV. All the exposure times are 47 s except for 48 s at 21:42:30. All the fluxes are in units of 10^{-8} erg cm^{-2} s^{-1}. The photon index of 1.85 with no error is a fixed value. Note all errors given are 1σ.

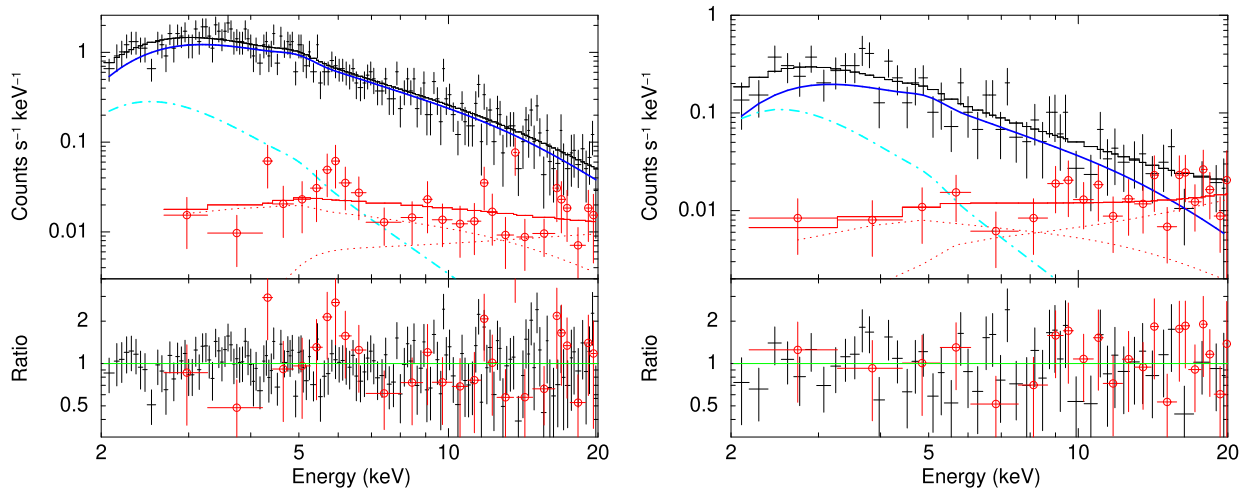

Figure 12. GSC spectra at $T_0 + 2.5$ ks (left panel) and at $T_0 + 8.0$ ks (right). The blue solid lines show the direct power-law component with Γ free for the spectrum at $T_0 + 2.5$ ks and fixed at 1.85 at $T_0 + 8.0$ ks. The light blue dashed lines are the power-law model with $\Gamma = 3.94$. The red points and lines are background data and models, respectively. The background model is the sum of two power laws. The best-fit data to the model ratio is also shown in each panel.

scan spectrum tends to be harder than the second scan one in all the cases.

The differential scattering cross section has energy E and scattering angle θ_s dependence of approximately $\exp(-\alpha E^2\theta_s^2)$ for $\theta_s \ll 1$ where α is a constant of proportional to the square of the size of grain (e.g., Mauche & Gorenstein 1986). Thus, an actual dust scattered component is considered to have a harder spectrum than assumed here especially in the first and second scan observations. If the time and spectral evolution of the dust echo ring is understood, the fitting parameters can be more constrained. This is, however, beyond the scope of this paper. Finally, we note that if we assume $\Gamma = 3.5$ for the scattered power-law component we got a steeper photon index ($\Gamma = 1.75 \pm 0.14$) and a lower 0.3–10 keV absorbed flux of $5.76^{+0.82}_{-0.70} \times 10^{-8}$ erg cm^{-2} s^{-1} for the direct power-law component in the first scan spectrum.

Appendix E
Dust Echo Modeling

In order to examine the properties of the dust scattered echo, images were created from the XRT PC-mode event data over the 0.8–5.0 keV band, where the dust reprocessing cross section peaks. Given the scattered emission evolves radially with time, the images were initially extracted over per snapshot intervals (with typical exposures ranging from 0.3 to 1.6 ks), until the day 22 post trigger when per observation ID (ObsID) images were created (with exposures from 3.3 to 5.2 ks). Vignetting-corrected exposure maps were also generated, spanning the observing times for each image.

Radial profiles were then generated as follows. The GRB position was obtained on a per image basis by fitting the expected XRT PSF model (including a piled-up profile modification when required, as described in Evans et al. 2020) to the imaging data out to 47.″1 where the central source dominates. This position was then used as the location about which radial profiles were generated, initially in 2.″357 linear bins from 0.′79 to 13.′75 radius, following the removal of 12 faint point sources (with count rates less than 3.5×10^{-3} count s^{-1}, determined from 67 ks of late-time data ranging from $T_0 + 43$ to 64 days after the trigger). The central source profile was retained and combined with a nominal background level determined from late-time data to provide the nonhalo background estimate. Example radial profiles are shown in Figure 13, which shows the echo emission expanding and decreasing in intensity with time. Later profiles were stacked to increase signal to noise in the plot, with radial bins scaled so that radial bins correspond to the first profile in the set of stacked observations according to Equation (1) in order to align radial intensity features of different observations.

The plots show clear excess over the PSF from the afterglow emission by the point source, with each peak (i.e., each ring in the image) corresponding to a separate dust cloud along the line of sight.

Approximating the light curve of the prompt emission as a delta function, the radial intensity of the echo, at time $t = t_{\rm GRB} + \Delta t$, plotted in Figure 13 can be written as

$$I_{\rm echo} = \frac{2c \cdot n(D_{\rm Dust})}{\theta^2} \cdot \mathcal{F} \cdot \frac{d\sigma}{d\Omega} \cdot e^{-\tau_{\rm phot}} \qquad \text{(E1)}$$

where $n(D)$ is the dust volume density as a function of distance $D(\theta, \Delta t)$ along the line of sight for a given scattering angle θ and time since the burst Δt, and $\tau_{\rm phot}$ is the optical depth to photoelectric absorption along the line of sight. The observed radial intensity distribution is then given by the convolution of Equation (E1) with the telescope PSF.

The flux of a given cloud of column density N at distance D (used to perform the dist model fits) is given by (Heinz et al. 2016)

$$F = \frac{2\pi cN}{D} \cdot \mathcal{F} \cdot \frac{d\sigma}{d\Omega}. \qquad \text{(E2)}$$

Because the time delay from the prompt emission and the radius θ of each ring are known, Equation (E1) can be used to measure the product of burst fluence, density, and scattering cross section, and, with knowledge of the fluence and a model for the scattering cross section, we can, in principle, solve for the dust density distribution $n_{\rm dust}$ as a function of line-of-sight (LOS) distance and the azimuthal angle along the ring for each observation.

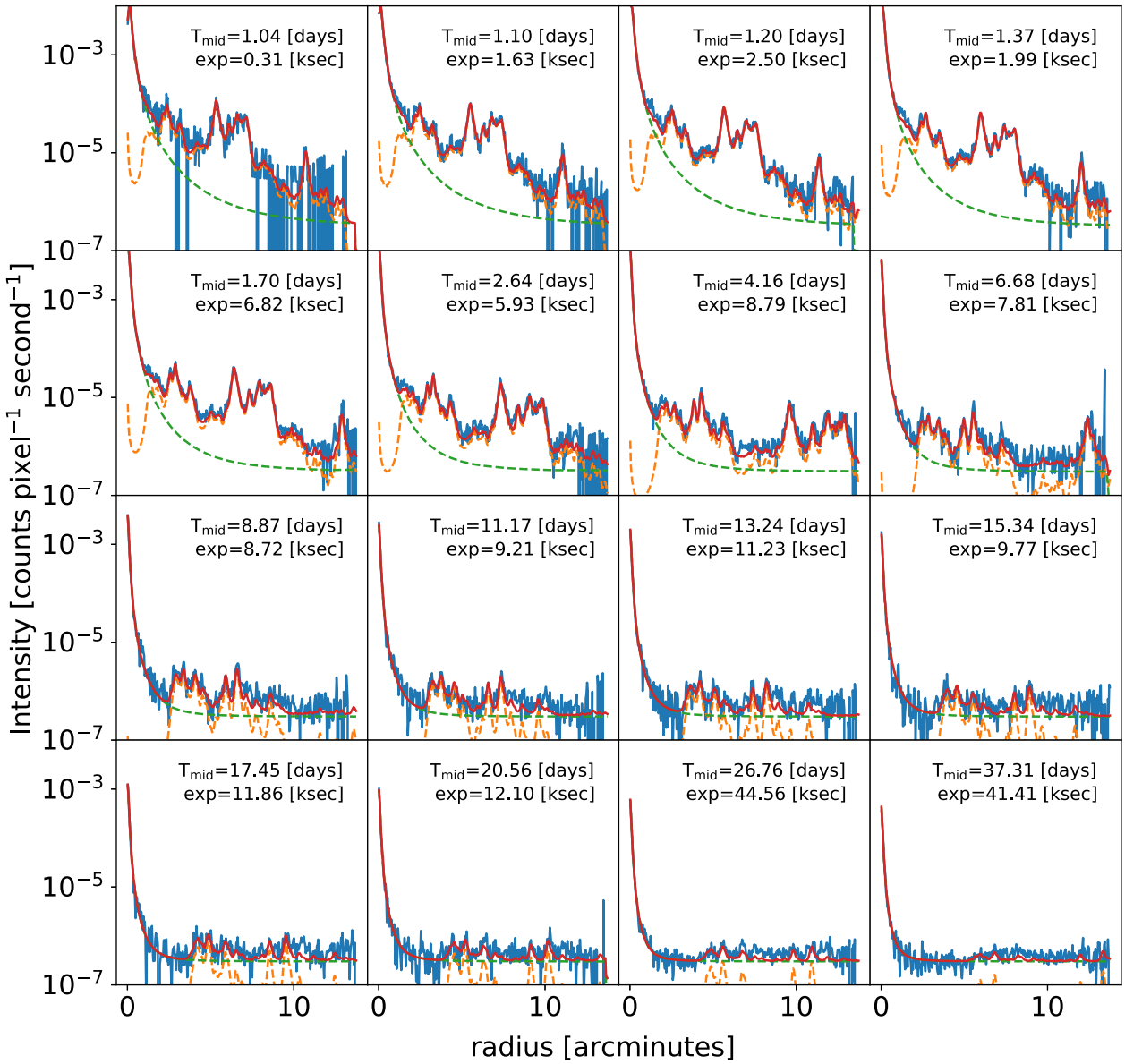

Figure 13. XRT PC-mode radial intensity profiles in the 0.8–5.0 keV band (blue solid lines); later profiles show stacked observations in indicated time windows, with radii scaled to the beginning of the observing window using Equation (1) so that radial intensity features at the same distance appear at the same radius. Overplotted lines show the PSF and background model (green dashed) and the dust model (orange dashed) and the best-fit model (solid red).

In practice, estimating the fluence at soft X-ray energies (where dust scattering is most efficient and where the echo is observed) requires extrapolation from the sensitivity band of the instruments that detected the prompt emission (namely, GBM; S. Lesage et al. 2023, in preparation), corrected for intrinsic absorption. This fluence value, derived using GBM data (after pile-up correction procedures), has an uncertainty of ∼50% that propagates to our results.

In addition, models for the dust scattering cross section vary from cloud to cloud and are themselves not well constrained. Thus, a conservative approach will treat both $d\,\sigma/d\Omega$ and $n_{\rm Dust}$ as functions to be fitted simultaneously, with the understanding that constraints derived for each will carry some degeneracy.

That said, the *relative* column density distribution is well constrained by this process, provided that dust chemistry and grain size distribution do not vary drastically from cloud to cloud.

At typical soft X-ray energies around 2 keV, the scattering cross section is roughly constant at angles smaller than about 100″ while falling off rapidly at larger scattering angles (roughly as $d\,\sigma/d\Omega \propto \theta^{3.5}$). This results in a rapid decline in the intensity and flux of the echo as a function of time as the ring size expands, as can be seen in Figure 13. It further implies that, beyond a ring radius of about 100″, smaller rings, which are farther away, will have a larger intensity per column density compared to larger rings, which are closer to the observer.

On the other hand, the Galactic latitude of GRB 221009A of $b = 4.^{\circ}3$ suggests that the Galactic column density distribution should be dominated by nearby dust within the plane, within a few kiloparsecs. For example, the dust at the intersection of the

LOS with the Solar circle on the far side of the Galaxy would lie 780 pc (almost 8 dust scale heights, e.g., Li et al. 2018) above the Galactic plane, where we would not expect to see substantial amounts of dust (however, any dust present at those distances will benefit from the intensity enhancement discussed in the previous paragraph).

To constrain the dust column density and cross section models, we decomposed the dust distribution along the line of sight into 100 logarithmically spaced bins and determined the least squares fit for the column density for each bin. To this end, we constructed 1D XRT PSFs to approximate the radial profile for each dust ring. We then defined the fitting function as given by Equation (E1) for each column density component. We added the point-source PSFs for each profile to the fitting function. We then fitted all 100 components simultaneously to all the background-subtracted and radial intensity profiles between days 1 and 42 post-burst. The resulting inferred density distribution is plotted in Figure 4.

Appendix F
Broadband SED Construction

The BAT survey spectra are produced using the `BatAnalysis` Python package (T. Parsotan et al. 2023, in preparation). Using the HEASoft `batsurvey` script, the `BatAnalysis` package calculates the count rate of the GRB in each of the 8 energy bins used in the BAT survey (14–20, 20–24, 24–35, 35–50, 50–75, 75–100, 100–150, and 150–195 keV) and the errors associated with each energy bin. The package also generates the detector response matrix using the HEASoft `batdrmgen` script for the BAT survey observation of interest.

For the time intervals of the two SEDs, we created time-sliced X-ray spectra being careful to limit dust echo contamination (see Section 3.2). The source spectral files were grouped to $\geqslant$20 counts per energy bin. The spectral files were normalized to correspond to the 0.3–10 keV flux of the afterglow at $T_0 + 4.2$ ks or $T_0 + 43$ ks. The flux used to normalize a given spectrum is determined by fitting a power law to the data within the SED time range, and the best-fit decay index is used to compute the flux at the mid-point of the SED, in the same way as was done for the UVOT data.

To build the optical spectral files, we follow the methodology provided in Schady et al. (2010). This essentially sets the count rates in the spectral files to that determined at an instantaneous epoch by extrapolating the UVOT light curves. In order to obtain the count rates at the instantaneous epoch, we first combined the data from the different filters into a single-flow light-curve filter. The light curves of the different filters were normalized to that in the v filter. The normalization was determined by fitting a power law to each of the light curves in a given time range simultaneously. The power-law indices were constrained to be the same for all the filters, and the normalizations were allowed to vary between the filters. The ratios of the power-law normalizations between each filter and the v filter were then used to shift the individual light curves to the same normalization as the v filter, thus resulting in a single filter light curve. To construct the two SEDs at $T_0 + 4.2$ ks and $T_0 + 43$ ks, we first determine the temporal slope from the single filter light curve within the corresponding time interval. By fixing the power-law index at this value, we then fit a power law to the individual filter light curves. We use the derived normalizations to compute the count rate and count-rate error at the required time, which was then applied to the relevant spectral file.

Appendix G
BAT Trigger Simulation

To estimate the intrinsic rate of such events, we utilize the BAT trigger simulator (Lien et al. 2014) to calculate the detectability of the prompt emission at different redshifts under different representative instrumental setups. Specifically, our setup uses (1) one standard average background level, (2) four different locations on the BAT image plane (i.e., Grid IDs of [14, 15, 16, 17] or equivalent boresight angles of [56°, 45°, 27°, 0°]), which represent different detector sensitivity and cover different locations within the BAT field of view, and (3) four different numbers of enabled detectors (29,000, 22,000, 18,000, and 15,000; these numbers represent the change of average number of enabled detectors from 2005 to 2022). We ran simulations with a combination of each of these setups with a sample of redshifts from $z = 0.1$, to $z = 12$, with increments of $\Delta z = 1.0$ (i.e., $z = 0.1$, 1.0, 2.0,...,12.0). The simulation results are summarized in Table 8.

For each setup, we estimate the expected number of detections based on the highest detectable redshift $z_{\rm lim}$ and an assumed intrinsic rate with the following equation:

$$N_{{\rm det},i_{\rm setup}} = R_{\rm GRB}(z < z_{\rm lim})\, f_{\rm survey}\, f_{\rm fov}\, f_{\rm grid}\, f_{\rm ndet}\,. \tag{G1}$$

$R_{\rm GRB}(z < z_{\rm lim})$ is the all-sky intrinsic rate up to the redshift limit for this burst to be detected by BAT with a specific setup of Grid ID and number of enabled detectors, and is calculated by integrating the comoving rate by taking into account of the volume of the universe through the following equation (see, e.g., Lien et al. 2011, for details of the derivation):

$$R_{\rm GRB}(z < z_{\rm lim}) = 4\pi \int_0^{z_{\rm limit}} R_{\rm GRB,comov}(z=0) \times \frac{r_{\rm comov}^2}{(1+z)} \frac{dr_{\rm comov}}{dz}\, dz, \tag{G2}$$

where the comoving distance $r_{\rm comov}(z) = (\frac{C}{H_0}) \int_0^z 1/H(z)\, dz$. $f_{\rm survey}$ is the fraction of time that BAT is capable of triggering, and we adopt $f_{\rm survey} = 0.8$ based on the study in Lien et al. (2016). $f_{\rm fov} = (2.1\ {\rm sr})/(4\pi\ {\rm sr})$ is the fraction of sky covered by the entire BAT field of view down to a partial coding fraction of $\sim$0.1, and $f_{\rm grid} = [0.460, 0.346, 0.109, 0.085]$ is the fraction of BAT field of view for Grid IDs (14), (15), (16), and (17).[46] In other words, $f_{\rm fov} \times f_{\rm grid}$ is the fraction of bursts in the entire sky that would have the partial coding fraction of the specific Grid ID. $f_{\rm ndet}$ is the fraction of GRBs in the BAT field of view that would occur with this number of enabled detectors. For simplicity, we assume an equal number of GRBs occur with these four numbers of enabled detectors. That is, $f_{\rm ndet} = 0.25$.

The total number of detections can then be calculated by adding up $N_{{\rm det},i_{\rm setup}}$ for all 16 combinations of instrumental

[46] https://asd.gsfc.nasa.gov/Craig.Markwardt/bat-cal/solid-angle/

Table 8
Detectable Redshift Limit for Each Instrumental Setup

Grid ID	ndet	$z_{\rm lim}$
17	29000	11
17	22000	11
17	18000	11
17	15000	11
16	29000	11
16	22000	11
16	18000	11
16	15000	11
15	29000	11
15	22000	10
15	18000	9
15	15000	9
14	29000	5
14	22000	4
14	18000	4
14	15000	3

Note. "Grid ID" indicates the location at the BAT image plane and corresponds to different partial coding fractions and thus different detector sensitivities. "ndet" refers to the number of enabled detectors.

setups listed in Table 8. That is,

$$N_{\rm det,tot} = \sum_{i_{\rm setup}=1}^{16} N_{{\rm det},i_{\rm setup}}. \quad \text{(G3)}$$

We assume a flat intrinsic comoving rate of $R_{\rm GRB,comov}(z=0)$ and adjust the value until the detection rate matches with that of a GRB 221009A–like event. We set the upper limit of the BAT detection rate of such events to be 1 per 18 yr of the Swift mission lifetime, because the prompt emission of the burst actually occurred outside of the BAT field of view. This gives us a corresponding upper limit of $R_{\rm GRB,comov}(z=0) \leqslant 6.1\times10^{-4}\,{\rm Gpc^{-3}\,yr^{-1}}$. Integrating this flat comoving rate from $z=0$, to $z=12$, we obtain an upper limit on the all-sky rate of GRB 221009A–like events to be $0.5\,{\rm yr^{-1}}$. Comparing to the all-sky intrinsic long-GRB rate of $\sim4571\,{\rm yr^{-1}}$ in Lien et al. (2014), the fraction of GRB 221009A–like events is roughly $0.5/4571 \leqslant 1.0\times10^{-4}$.

ORCID iDs

Maia A. Williams https://orcid.org/0000-0002-0025-3601
Jamie A. Kennea https://orcid.org/0000-0002-6745-4790
S. Dichiara https://orcid.org/0000-0001-6849-1270
Wataru B. Iwakiri https://orcid.org/0000-0002-0207-9010
Andrew P. Beardmore https://orcid.org/0000-0001-5186-5950
P. A. Evans https://orcid.org/0000-0002-8465-3353
Sebastian Heinz https://orcid.org/0000-0002-8433-8652
Amy Lien https://orcid.org/0000-0002-7851-9756
S. R. Oates https://orcid.org/0000-0001-9309-7873
Hitoshi Negoro https://orcid.org/0000-0003-0939-1178
S. Bradley Cenko https://orcid.org/0000-0003-1673-970X
Douglas J. K. Buisson https://orcid.org/0000-0002-5341-6929
Dieter H. Hartmann https://orcid.org/0000-0002-8028-0991
Gaurava K. Jaisawal https://orcid.org/0000-0002-6789-2723
N. P. M. Kuin https://orcid.org/0000-0003-4650-4186
Stephen Lesage https://orcid.org/0000-0001-8058-9684
Kim L. Page https://orcid.org/0000-0001-5624-2613
Tyler Parsotan https://orcid.org/0000-0002-4299-2517
Dheeraj R. Pasham https://orcid.org/0000-0003-1386-7861
B. Sbarufatti https://orcid.org/0000-0001-6620-8347
Michael H. Siegel https://orcid.org/0000-0003-1817-3009
George Younes https://orcid.org/0000-0002-7991-028X
Elena Ambrosi https://orcid.org/0000-0002-9731-8300
M. G. Bernardini https://orcid.org/0000-0001-6106-3046
S. Campana https://orcid.org/0000-0001-6278-1576
Milvia Capalbi https://orcid.org/0000-0002-9558-2394
Regina Caputo https://orcid.org/0000-0002-9280-836X
Antonino D'Aì https://orcid.org/0000-0002-5042-1036
P. D'Avanzo https://orcid.org/0000-0001-7164-1508
V. D'Elia https://orcid.org/0000-0002-7320-5862
Massimiliano De Pasquale https://orcid.org/0000-0002-4036-7419
R. A. J. Eyles-Ferris https://orcid.org/0000-0002-8775-2365
Elizabeth Ferrara https://orcid.org/0000-0001-7828-7708
Keith C. Gendreau https://orcid.org/0000-0001-7115-2819
Jeffrey D. Gropp https://orcid.org/0000-0002-9090-5553
Nobuyuki Kawai https://orcid.org/0000-0001-9656-0261
Noel Klingler https://orcid.org/0000-0002-7465-0941
Sibasish Laha https://orcid.org/0000-0002-2002-6350
A. Melandri https://orcid.org/0000-0002-2810-2143
Tatehiro Mihara https://orcid.org/0000-0002-6337-7943
Michael Moss https://orcid.org/0000-0002-1103-7082
Paul O'Brien https://orcid.org/0000-0002-5218-1899
Julian P. Osborne https://orcid.org/0000-0002-1041-7542
David M. Palmer https://orcid.org/0000-0001-7128-0802
Matteo Perri https://orcid.org/0000-0003-3613-4409
E. Sonbas https://orcid.org/0000-0002-6909-192X
Michael Stamatikos https://orcid.org/0000-0001-7253-8553
Rhaana Starling https://orcid.org/0000-0001-5803-2038
G. Tagliaferri https://orcid.org/0000-0003-0121-0723
Aaron Tohuvavohu https://orcid.org/0000-0002-2810-8764
Silvia Zane https://orcid.org/0000-0001-5326-880X
Houri Ziaeepour https://orcid.org/0000-0001-8164-3582

References

Arnaud, K. A. 1996, in ASP Conf. Ser. 101, Astronomical Data Analysis Software and Systems V, ed. G. H. Jacoby & J. Barnes (San Francisco, CA: ASP), 17
Astropy Collaboration, Robitaille, T. P., Tollerud, E. J., et al. 2013, A&A, 558, A33
Barthelmy, S. D., Barbier, L. M., Cummings, J. R., et al. 2005, SSRv, 120, 143
Beardmore, A. P., Willingale, R., Kuulkers, E., et al. 2016, MNRAS, 462, 1847
Bloom, J. S., Frail, D. A., & Sari, R. 2001, AJ, 121, 2879
Bloom, J. S., Perley, D. A., Li, W., et al. 2009, ApJ, 691, 723
Breeveld, A. A., Landsman, W., Holland, S. T., et al. 2011, in AIP Conf. Ser. 1358, ed. J. E. McEnery, J. L. Racusin, & N. Gehrels (Melville, NY: AIP), 373
Brethauer, D., Grefenstette, B., Racusin, J., et al. 2022, GCN, 32695, 1
Brown, P. J., Roming, P. W. A., Milne, P., et al. 2010, ApJ, 721, 1608
Burrows, D. N., Hill, J. E., Nousek, J. A., et al. 2005, SSRv, 120, 165
Campana, S., Mangano, V., Blustin, A. J., et al. 2006, Natur, 442, 1008
Cash, W. 1979, ApJ, 228, 939
Castro-Tirado, A. J., Sanchez-Ramirez, R., Hu, Y. D., et al. 2022, GCN, 32686, 1
Cenko, S. B., Frail, D. A., Harrison, F. A., et al. 2011, ApJ, 732, 29
D'Avanzo, P., Ferro, M., Brivio, R., et al. 2022, GCN, 32755, 1
De Pasquale, M., Evans, P., Oates, S., et al. 2009, MNRAS, 392, 153
de Ugarte Postigo, A., Izzo, L., Pugliese, G., et al. 2022, GCN, 32648, 1
Dichiara, S., Gropp, J. D., Kennea, J. A., et al. 2022, GCN, 32632, 1
Evans, P. A., Beardmore, A. P., Page, K. L., et al. 2007, A&A, 469, 379
Evans, P. A., Beardmore, A. P., Page, K. L., et al. 2009, MNRAS, 397, 1177
Evans, P. A., Page, K. L., Beardmore, A. P., et al. 2023, MNRAS, 518, 174

Evans, P. A., Page, K. L., Osborne, J. P., et al. 2020, ApJS, 247, 54
Foreman-Mackey, D., Farr, W., Sinha, M., et al. 2019, JOSS, 4, 1864
Frail, D. A., Kulkarni, S. R., Sari, R., et al. 2001, ApJL, 562, L55
Galama, T. J., Vreeswijk, P. M., van Paradijs, J., et al. 1998, Natur, 395, 670
Gehrels, N., Chincarini, G., Giommi, P., et al. 2004, ApJ, 611, 1005
Gendreau, K. C., Arzoumanian, Z., & Okajima, T. 2012, Proc. SPIE, 8443, 844313
Ghisellini, G., Ghirlanda, G., Nava, L., & Firmani, C. 2007, ApJL, 658, L75
Guha, A., & Nicholson, P. 2022, GCN, 32745, 1
Heinz, S., Burton, M., Braiding, C., et al. 2015, ApJ, 806, 265
Heinz, S., Corrales, L., Smith, R., et al. 2016, ApJ, 825, 15
Huang, Y., Hu, S., Chen, S., et al. 2022, GCN, 32677, 1
Iwakiri, W., Jaisawal, G. K., Younes, G., et al. 2022, GCN, 32694, 1
Izzo, L., Saccardi, A., Fynbo, J. P. U., et al. 2022, GCN, 32765, 1
Kann, D. A., Agayeva, S., Aivazyan, V., et al. 2023, arXiv:2302.06225
Kann, D. A., & Agui Fernandez, J. F. 2022, GCN, 32762, 1
Kennea, J. A., Williams, M. & Swift Team 2022, GCN, 32635, 1
Kobayashi, K., Negoro, H., Nakajima, M., et al. 2022, GCN, 32756, 1
Kuin, N. P. M., Dichiara, S. & Swift/UVOT Team 2022, GCN, 32656, 1
Kulkarni, S. R., Frail, D. A., Wieringa, M. H., et al. 1998, Natur, 395, 663
Laha, S., Wadiasingh, Z., Parsotan, T., et al. 2022, ApJ, 929, 173
Laskar, T., Alexander, K. D., Margutti, R., et al. 2023, arXiv:2302.04388
Levan, A. J., Lamb, G. P., Schneider, B., et al. 2023, arXiv:2302.07761
Li, L., Shen, S., Hou, J., et al. 2018, ApJ, 858, 75
Lien, A., Chakraborty, N., Fields, B. D., & Kemball, A. 2011, ApJ, 740, 23
Lien, A., Sakamoto, T., Barthelmy, S. D., et al. 2016, ApJ, 829, 7
Lien, A., Sakamoto, T., Gehrels, N., et al. 2014, ApJ, 783, 24
Liu, Y.-Q., Modjaz, M., Bianco, F. B., & Graur, O. 2016, ApJ, 827, 90
Margutti, R., Milisavljevic, D., Soderberg, A. M., et al. 2014, ApJ, 797, 107
Maselli, A., Melandri, A., Nava, L., et al. 2014, Sci, 343, 48
Mathis, J. S., Rumpl, W., & Nordsieck, K. H. 1977, ApJ, 217, 425
Matsuoka, M., Kawasaki, K., Ueno, S., et al. 2009, PASJ, 61, 999
Mauche, C. W., & Gorenstein, P. 1986, ApJ, 302, 371
Meegan, C., Lichti, G., Bhat, P. N., et al. 2009, ApJ, 702, 791
Mihara, T., Nakajima, M., Sugizaki, M., et al. 2011, PASJ, 63, S623
Morgan, A. N., Perley, D. A., Cenko, S. B., et al. 2014, MNRAS, 440, 1810
Nasa High Energy Astrophysics Science Archive Research Center (Heasarc) 2014, HEAsoft: Unified Release of FTOOLS and XANADU, Astrophysics Source Code Library, ascl:1408.004
Negoro, H., Kohama, M., Serino, M., et al. 2016, PASJ, 68, S1
Negoro, H., Nakajima, M., Kobayashi, K., et al. 2022, ATel, 15651, 1
Negro, M., Di Lalla, N., Omodei, N., et al. 2023, arXiv:2301.01798
Nousek, J. A., Kouveliotou, C., Grupe, D., et al. 2006, ApJ, 642, 389
Oates, S. R., Page, M. J., Schady, P., et al. 2009, MNRAS, 395, 490
O'Connor, B., Troja, E., Ryan, G., et al. 2023, arXiv:2302.07906
Perley, D. A., Cenko, S. B., Corsi, A., et al. 2014, ApJ, 781, 37
Piran, T. 2004, RvMP, 76, 1143
Planck Collaboration, Aghanim, N., Akrami, Y., et al. 2020, A&A, 641, A6
Poole, T. S., Breeveld, A. A., Page, M. J., et al. 2008, MNRAS, 383, 627
Racusin, J. L., Liang, E. W., Burrows, D. N., et al. 2009, ApJ, 698, 43
Remillard, R. A., Loewenstein, M., Steiner, J. F., et al. 2022, AJ, 163, 130
Roming, P. W. A., Kennedy, T. E., Mason, K. O., et al. 2005, SSRv, 120, 95
Sari, R., Piran, T., & Halpern, J. P. 1999, ApJL, 519, L17
Sari, R., Piran, T., & Narayan, R. 1998, ApJL, 497, L17
Schady, P., Mason, K. O., Page, M. J., et al. 2007, MNRAS, 377, 273
Schady, P., Page, M. J., Oates, S. R., et al. 2010, MNRAS, 401, 2773
Schlafly, E. F., & Finkbeiner, D. P. 2011, ApJ, 737, 103
Schnoor, P. W., Nicholson, P., & Welch, D. L. 2022, GCN, 32744, 1
Siegel, M. H., Porterfield, B. L., Linevsky, J. S., et al. 2014, AJ, 148, 131
Sugizaki, M., Mihara, T., Serino, M., et al. 2011, PASJ, 63, S635
Tiengo, A., Pintore, F., Mereghetti, S., & Salvaterra, R. 2022, ATel, 15661, 1
Vasilopoulos, G., Karavola, D., Stathopoulos, S. I., & Petropoulou, M. 2023, MNRAS, Advance Access
Vasilopoulos, G., & Petropoulou, M. 2016, MNRAS, 455, 4426
Veres, P., Burns, E., Bissaldi, E., et al. 2022, GCN, 32636, 1
Willingale, R., Starling, R. L. C., Beardmore, A. P., Tanvir, N. R., & O'Brien, P. T. 2013, MNRAS, 431, 394
Yamazaki, R., Sato, Y., Sakamoto, T., & Serino, M. 2020, MNRAS, 494, 5259
Zhang, B., Fan, Y. Z., Dyks, J., et al. 2006, ApJ, 642, 354